Ólafsson, Dagur; Vilaça, Pedro; Vesanko, Jussi

Multiphysical characterization of FSW of aluminum electrical busbars with copper ends

Published in:
Welding in the World

DOI:
10.1007/s40194-019-00814-0

Published: 01/01/2020

Document Version
Publisher's PDF, also known as Version of record

Welding in the World
https://doi.org/10.1007/s40194-019-00814-0

RESEARCH PAPER

Multiphysical characterization of FSW of aluminum electrical busbars with copper ends

Dagur Ólafsson [1,2] · Pedro Vilaça [1] · Jussi Vesanko [3]

Received: 30 June 2019 / Accepted: 5 October 2019

Abstract
This work investigates the benefits of having an aluminum (Al) busbar with welded copper (Cu) ends, and evaluates the force relaxation phenomena of a pre-loaded bolt joint on Cu versus Al, under cyclic thermal loading. The results show a force relaxation rate 50% lower in the Cu-bolted joint compared with the one in Al. The core of this research is the weldability analysis of Al-Cu butt joints made by friction stir welding (FSW). The materials are AA1050 H14/24 and Cu OF 04 with thickness of 6 mm. Temperature monitoring during the FSW cycle emphasize how heat generation depends mostly on local internal viscoplastic deformation. Tensile, bending, and microhardness tests were used to establish the mechanical properties. Optical microscope and scanning electron microscopy were used to characterize the microstructure. Joining mechanisms in the weld were investigated using energy-dispersive X-ray spectroscopy. The FSW resulted in 85% tensile strength efficiency compared to the Al base material, and 97% electrical conductivity efficiency compared to an ideal bimetallic component made of the same materials with no contact resistance. Electrical resistance of the FSW is 200 times lower than the electrical contact resistance between the Al-Cu materials while under high compressive force.

Keywords Friction stir welding · Aluminum · Copper · Busbar · Electrical resistance · Temperature · Microstructure · Intermetallic compounds · Mechanical properties

1 Introduction

Various industries constantly strive to improve their competitiveness, with higher performance products made with efficient processes with low environmental impact. Most of the developments are supported by material optimization demanding advanced solution for manufacturing, where joining of dissimilar engineering materials is typically the most challenging process. On this scope, the friction stir welding (FSW) [1] is a modern solid-state material joining technique, which opens up possibilities in manufacturing joints of dissimilar materials that are difficult, or even impossible, to do with conventional fusion welding methods. Due to high forces, the process is fully mechanized enabling high productivity for high production series, lowering the depended on skill requirements and thus cost of operation [2]. In FSW, the heat is mostly generated by friction dissipation during the internal plastic deformation, and thus the materials do not reach their melting temperatures as the local heat generation is reduced to zero as the increasing temperature tends to melting [3, 4]. This means that when FSW of dissimilar materials, the local temperature is the one enabling the local viscoplastic deformation imposed by the rigid tool, clamping conditions, and process parameters. This same phenomenon is later emphasized in this paper, based on the results from the monitoring of the temperatures during the FSW of the Al-Cu joints. Good quality FSW bimetallic joints are now feasible for Al to steel [5–7] and Al to Cu [8]. Avoiding common problems associated with fusion welding of dissimilar metals, such as mismatch of fusion temperature, formation of extensive brittle intermetallic compounds (IMC's), gas solubility, and high distortion, and residual stress [2], the FSW opened up new possibilities in the design optimization and manufacturing of various products. In particular, electrical applications such as the busbars can get significant benefits from combining cheaper and lighter

✉ Pedro Vilaça
pedro.vilaca@aalto.fi

[1] Department of Mechanical Engineering, School of Engineering, Aalto University, Espoo, Finland

[2] Innovation Center Iceland, Reykjavík, Iceland

[3] Promeco Oy, Kankaanpää, Finland

Published online: 04 November 2019

material, such as Al, with Cu that has lower electrical resistance, with more stable mechanical properties and corrosion resistance in a wider temperature range.

Busbars are conductive strips or bars used for short distance high current power transference. In recent years, the material choice for busbars has been changing from Cu to Al. This is due to the lower price and higher conductivity of the Al when considered on a per kilogram basis [9]. The decrease in the direct cost and weight of the busbar is attractive, but perhaps short-sighted. High clamping forces are required for busbar connections to minimize the contact resistance between the busbars and other components [10]. These high forces, along with the temperature, change the connection experience, while in operation slowly deform the pressed material, which in turn lowers the clamping forces. High thermal expansion and oxidation of the Al further degrade the electrical connection [11]. To avoid component failure, the connection therefore needs to be retightened periodically. This results in maintenance costs, and increases the life cycle price of the Al busbar.

Elevated temperatures affect Al alloys commonly used for busbars such as AA6101-T4 more than high conductive Cu alloys like Cu-OF [12, 13]. The thermal expansion coefficient is also higher for Al than for Cu [14]. These differences between the two materials might explain the higher maintenance associated with Al busbars. A potential solution to this problem is to use bimetallic busbars made from both materials, Al and Cu. A busbar mainly composed of Al but with Cu ends has the advantage of being cheaper and lighter than a monolithic Cu busbar but avoids the increase in maintenance cost associated with monolithic Al busbars. Additionally, Cu ends are more suitable for clamped connections with other Cu parts in an electrical system than Al/Cu- or Al/Al-bolted connections [15, 16]. For this solution to be viable, these bimetallic busbars need to be manufactured efficiently.

Difference in fusion temperatures, as between Cu and Al, is not a problem for the FSW, but several other issues remain contributing for the Al-Cu made by FSW to be a challenging joint, still demanding research on the influence of the FSW conditions on the joint properties. Among these issues are the different deformation behaviors, formation of IMCs even at low temperatures, and differences in physical properties and their evolution with temperature, promoting asymmetry in the flow of material and heat during the FSW [17]. The IMCs are defined as solid phases containing two or more metallic elements, with optionally one or more non-metallic elements, whose crystal structure differs from that of the other constituents [18]. They are generally very stable, brittle, and with a high fusion temperature, causing a problem in the welding of dissimilar materials, both in fusion and solid-state welding. In fusion welding, they are generally formed during the solidification of the welding pool. In FSW, they form under high pressures and intense plastic deformation [19] under the heating of the welded joint. In fusion welding of dissimilar materials, the amount of intermetallic compounds is so that it compromises the weld in almost every case and renders the welding method useless for many material combinations such as Al and Cu [20].

In this work, the difference in force relaxation rates between Cu-OF-04 and strain-hardened AA6101-T4 under a 40 kN clamping force from a bolt while under cyclic thermal loading, simulating a busbar connection while in operation, is investigated to learn about the effective level of benefit in producing Al-busbar with Cu ends, as represented in Fig. 1. The weldability analysis focuses on the FSW of the bimetallic joint between plates with thickness of 6 mm made of AA1050-H14/24 and Cu-OF-04. The Al material in the FSW joint was selected to maximize the electrical conductivity (where $\sigma_{Cu\text{-}OF} \cong 100\%$ IACS; $\sigma_{AA1050} \cong 61\%$ IACS; and $\sigma_{AA6101} \cong 43\%$ IACS), because there is no need for higher mechanical resistance, as provided by AA6101-T4, when the busbar ends are made of Cu. During the FSW, the temperatures were monitored. Tensile, bending, and microhardness tests were used to establish the mechanical properties. Optical microscope and scanning electron microscope were used to investigate the microstructure. The electrical resistance of the Al-Cu weld and contacting Al-Cu components under different clamping force levels was assessed using a microhmmeter.

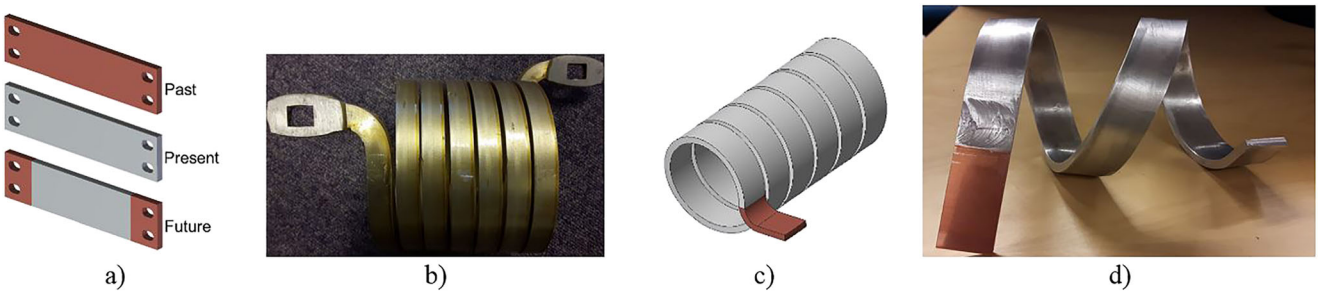

Fig. 1 Scope and concept of the aluminum-based busbar (Al-busbar) with welded copper (Cu) ends: (a) evolution of the material selection for the busbars to link electrical power systems; (b) an example of an industrial busbar made of aluminum; (c) schematic concept of the busbar with a welded copper end; (d) implementation with the FSW conditions investigated in this research work

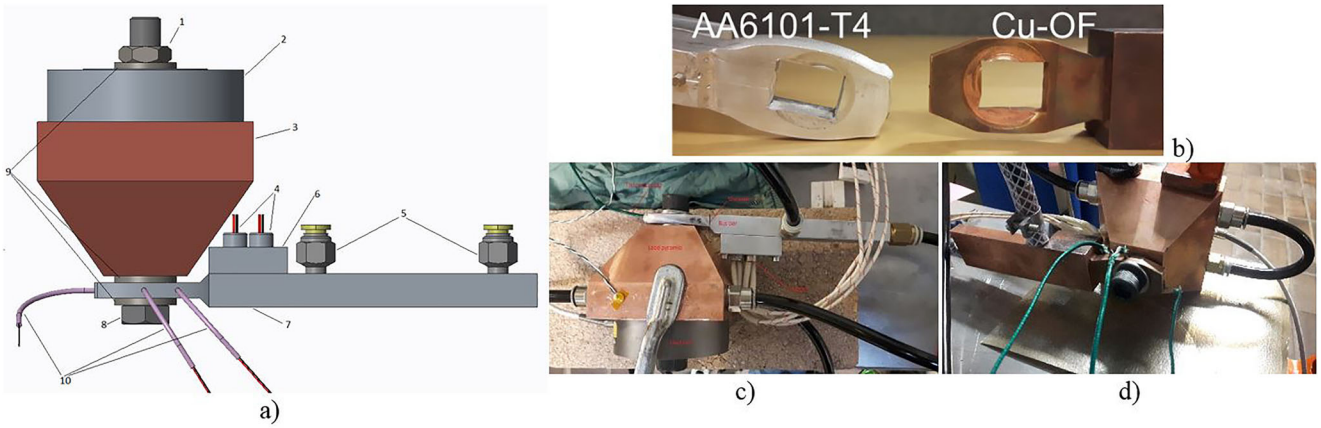

Fig. 2 Experimental setup of the clamping force relaxation experiment: (a) schematic representation of the components where 1, 8, and 9 are M12 nut, bolt, and stainless steel washers, respectively; 2, load cell; 3, load pyramid; 4 and 6, cartridge heaters and socket, respectively; 5, cooling connectors; 7, busbar end; 10, thermocouples. (b) Tested busbar ends made of AA6101-T4 and Cu-OF-04. (c), (d) Testing apparatus for the AA6101-T4 and Cu-OF-04, respectively

2 Evaluation of the clamping force relaxation

2.1 Experimental conditions and methods

The experimental setup, presented in Fig. 2, is made of several parts. A strain-gauge load cell and the busbar end are clamped together between a bolt and a nut, separated by stainless steel washers and a load pyramid, which transfers the load from the larger load cell to the small end of the bus bar. Behind the flattened mounting end of the bus bar, cartridge heaters are placed and an internal cooling channel was made. To monitor the thermal cycles in the investigated zone, three K-type thermocouple wires are welded to the flattened end part of both the Cu and Al testing specimens. These thermocouples are positioned near the edge of the flattened end part, around and equidistant from the clamping system. Three thermocouples are used to be sure about the uniform thermal distribution in the zone under investigation and for matter of redundancy of the information. The flattened part of the Cu component is machined with an $HV05_{Cu\text{-}OF} \cong 88$; the flattened part of the Al component is forged reaching an $HV05_{AA6101\_FlattenedEnd} \cong 90$, from the original base material hardness of $HV05_{AA6101\text{-}T4} \cong 60$.

The test was controlled and conducted as follows: the force and temperature monitoring is activated and the data is sampled and logged with certain sampling frequencies, f_F and f_T. The bolt is preloaded with a certain force, F_0, and the cooling flow is turned on. Then an iterative cycle begins. The heaters are turned on for a certain amount of time, Δt_{Hot}, allowing the temperature of the busbar end to reach T_{Hot}. Then, the heaters are turned off for a certain amount of time, Δt_{Cold}, allowing the temperature to reach T_{Cold}. If either the number of cycles has reached a certain maximum, N_{max}, or the force is under a certain minimum, F_{min}, the cooling flow is turned off, the test is stopped, and the data is analyzed. Otherwise, the process goes through another iterative cycle. The flowchart in Fig. 3 further depicts the test protocol. Tests were run for each material using a peak temperature of 190 ± 5 °C. The peak

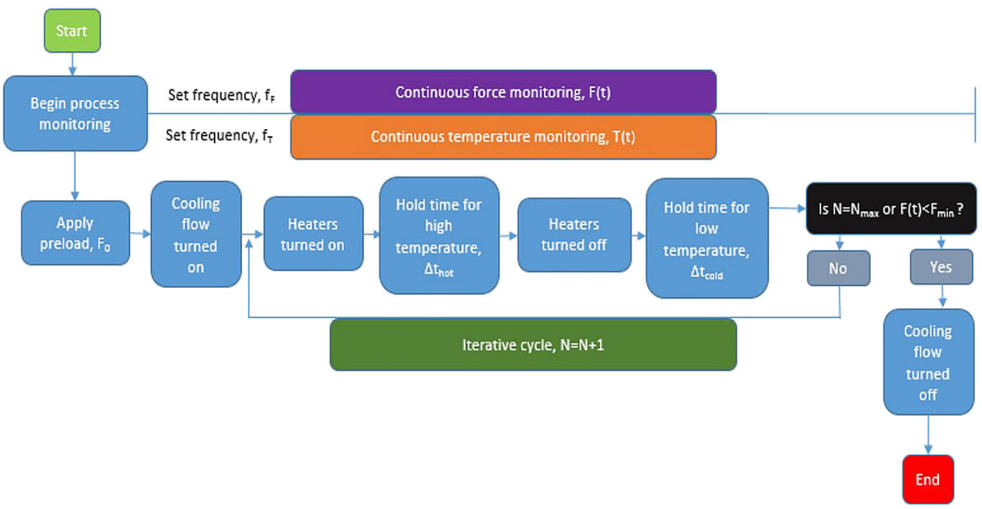

Fig. 3 Test protocol for the clamping force relaxation experiment

Table 1 Summary of the results of the clamping force relaxation test detailing the clamping force at different cycles as well as the average rate in clamping force between cycles 100–200 for each material

$T_{max}/\Delta T$	Material	$F_{@300\ cycles}$	$F_{@800\ cycles}$	$\Delta F/cycle_{@100–200\ cycles}$
190 °C/60 °C	Cu-OF-04	33.8 kN	33.2 kN	− 4.2 N
	AA6101-T4	26.5 kN	25.3 kN	− 8.1 N

temperature considered is the temperature measured by the thermocouple closest to the source of the heat, i.e., the cartridge heaters. The sampling frequencies f_F and f_T were both 1 Hz. The heating cycle was so that the heaters were on for 50 s and off for 20 s. Both experiments used a preload force of 40 kN. The contact surface area between the washers and the busbar ends was estimated to be 230 mm^2; thus, the initial contact pressure is estimated as 170 MPa.

2.2 Results

The clamping force relaxes at a higher rate for AA6101-T4 than for Cu-OF-04. From the original 40 kN, the clamping force in the Al lowers to 25.2 kN after 881 cycles while the force on the Cu lowers to 32.9 kN after 1236 cycles. Table 1 depicts the clamping force in the tests at 300 and at 800 cycles as well as the average rate of drop of the clamping force per cycle between 100 and 200 cycles. The reference rate of the clamping force relaxation measured was $\Delta F/cycle_{@100–200\ cycles} = -4.2$ N for the Cu-OF-04 and $\Delta F/cycle_{@100–200\ cycles} = -8.1$ N for the AA6101-T4. From Fig. 4, where it is presented the evolution of the clamping force along the whole thermal fatigue test, it is possible to conclude that the relaxation rates of the clamping force are higher at start of the test, when higher clamping forces are present, and that the relation between the relaxation rates exhibited by the Al and the Cu end busbar components remains essentially constant during the whole test at about the double.

Plot of the clamping force *versus* time for both the AA6101-T4 and the Cu-OF-04. The detail focuses on the period of about 13 min, between the 50th and the 60th cycles. The relaxation rates exhibited by the Al component are about the double of the Cu end busbar component. The relaxation rates of the clamping force are higher at start of the test, when higher clamping forces are present. This phenomenon is probably induced by differences in yield strength at elevated temperatures and thermal expansion coefficients between the Al- and Cu-based materials. The AA6061 is probably overaged and loses its mechanical resistance in this range of temperature operation.

The threshold for preventive maintenance of the bolted clamping force will depend on the operation conditions and inherent interfacial electrical resistance for different levels of clamping force. These resistance values will be presented later in this paper. But immediately, whatever are the threshold criteria for maintenance operation, Cu ends for the busbar, will have a very significant benefit in increasing the preventive maintenance interval and overall safety of the electrical system operation.

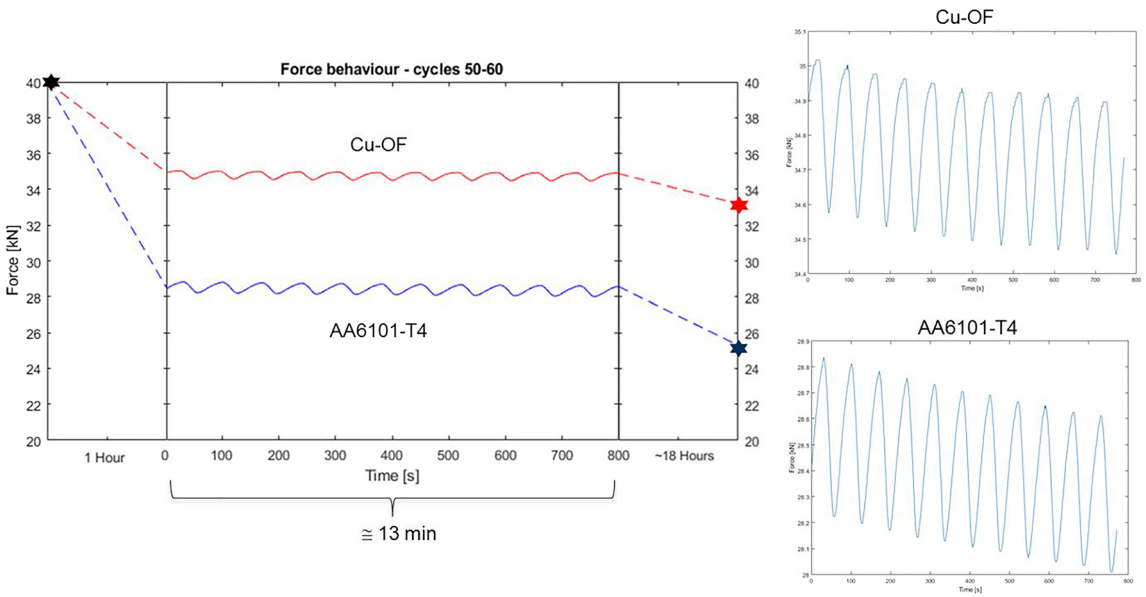

Fig. 4 Plot of the clamping force *versus* time for both the AA6101-T4 and the Cu-OF-04. The detail focuses on the period of about 13 min, between the 50th and the 60th cycles. The relaxation rates exhibited by the Al component are about the double of the busbar Cu end component. The relaxation rates of the clamping force are higher at start of the test, when higher clamping forces are present

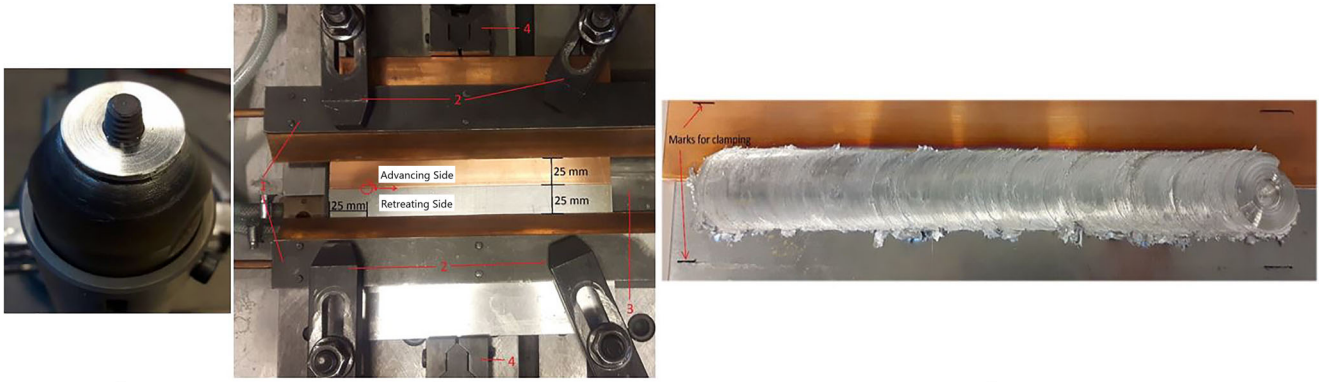

Fig. 5 The FSW welding conditions: (a) tool with a concave shoulder and taper LH-threaded probe; (b) the clamping system with the (1) refrigerated Cu clamping bars and (2) steel clamps, (3) refrigerated baking anvil, and (4) side stoppers; (c) perspective of the top surface of the Al-Cu joint in as-welded condition

3 Weldability analysis of the Al-Cu plate system

3.1 Experimental conditions and methods

Base materials The aluminum selected for the busbars was a rolled plate of AA1050-H14/H24, which is a highly conductive ($\sigma_{AA1050} \cong 61\%$ IACS) and commercial pure aluminum material (Al ≥ 99.5%). The Cu plate chosen is a high-purity, oxygen-free, non-phosphorus-deoxidized Cu alloy that does not contain any vacuum-evaporating elements. Generally, it is simply known as oxygen-free copper or Cu-OF ($\sigma_{Cu\text{-}OF} \cong 100\%$ IACS). The particular classification used during this work was Cu-OF-04. The thickness of all plates was 6 mm. The plates were prepared to be welded along the rolling direction (RD) and were cut with dimensions 250 mm (RD) × 60 mm. The hardness measured at top surface for the Al and Cu plates were $HV05_{AA1050} \cong 40$ and $HV05_{Cu\text{-}OF} \cong 88$, respectively.

Welding conditions and parameters The equipment used for the FSW was an ESAB Legio 5, in position control mode, because preliminary tests demonstrated that it is difficult to maintain the stability and thus repeatability in long welds of dissimilar materials under force control mode. The tooling, clamping system, and resulting welds are represented in Fig. 5. The tool used for the welds was selected after preliminary tests. It has Ø24 mm concave shoulder and Ø8 mm LH-threaded taper 5.6-mm long probe (Fig. 5a). While some of the welding parameters were selected based on literature review and preliminary tests, namely, the rotation speed, tilt angle, and dwell time, other key process parameters, namely, the travel speed, weld position, and lateral offset position of the tool in relation to the joint line between the base materials were obtained via DoE [21]. Three performance parameters were used to optimize the selected key process parameters via the DoE: "global efficiency to tensile strength", see Eq. (1), "global efficiency to bending", see Eq. (2), for the mechanical properties and the "Electrical conductivity efficiency", see Eq. (4), for assessment of the electrical performance which is

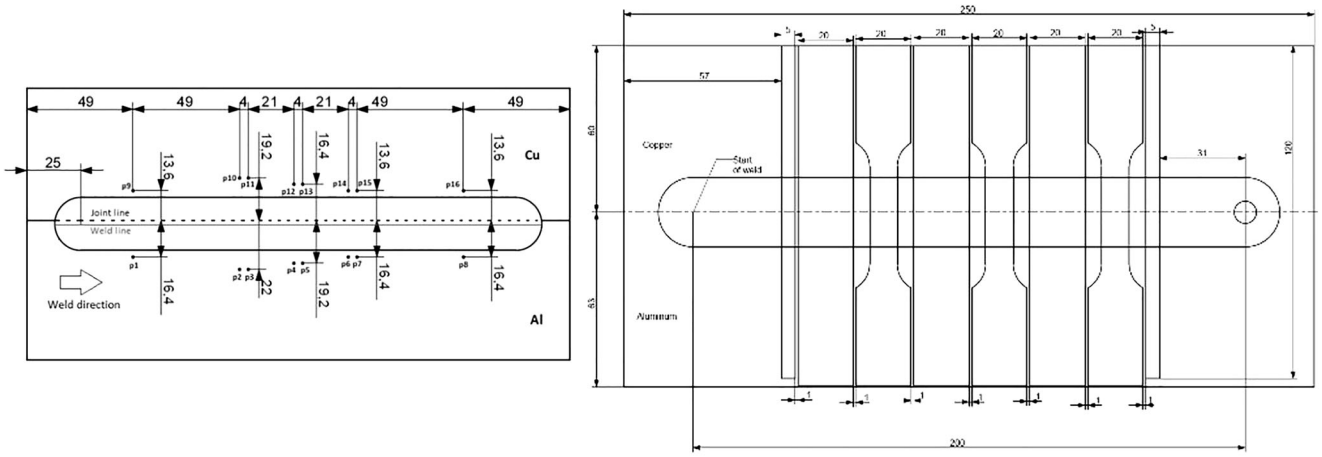

Fig. 6 Schematic representation of some planned research actions of the weld joint properties: (a) plan of the thermocouple positions for temperature monitoring; (b) specimen extraction plan for metallurgical, mechanical, and electrical tests. Dimensions in millimeters

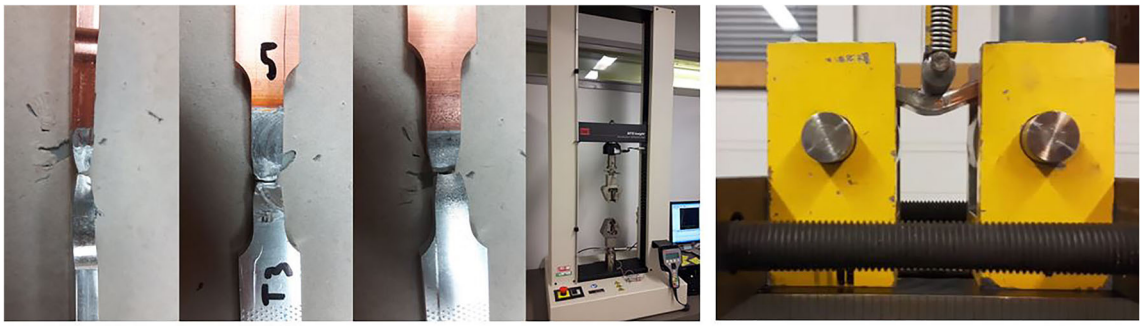

Fig. 7 Mechanical testing of the welded Al-Cu specimens: (a) three specimens tested for tensile strength with fracture surface outside of the original joint line interface; (b) bending test operation

an important parameter in the design of busbars. The FSW parameters implemented for this weldability analysis were rotational speed = 800 rpm (CW); travel speed = 125 mm/min; tool plunge position = 5.1 mm (leading to an average vertical forging force of about 9.5 kN); lateral offset into the Al side = 1.4 mm (revealed in the extraction hole of the tool probe in Fig. 5c); tilt angle = 2°; and dwell time = 5 s. The Cu was placed on the advancing side of the welds as depicted in Fig. 5b.

The welds were produced with 200 mm in length, along the rolling direction of the Al-Cu plates, starting and ending 25 mm away from the plate edges, as represented in Fig. 6. The specimens for bending, tensile, optical microscopy (OM), microhardness mapping, scanning electron microscopy (SEM), energy dispersive X-ray spectroscopy (EDS), and electrical resistance test specimen were extracted from the 200-mm long optimized AA1050-H14/24–Cu-OF-04 FSW welds.

Temperature monitoring Sixteen thermocouples K-type with Ø 0.8 mm were positioned in drilled holes with Ø1.0 mm at mid-plate thickness depth, i.e., 3 mm. Thermal paste was used for improved thermal conductivity and epoxy adhesive was applied to keep them stable. The thermocouples were positioned as represented in Fig. 6a. The strategical position was so that the thermocouples on each side were at same distance from the center of the stirred zone. The thermocouples were placed inside these holes. During the weld process, some of the thermocouples, especially on the Al side, were pushed away by the flash formed during the weld and their data is not considered for further evaluation (Fig. 9a, c).

Microstructural analysis Specimens for optical microscopy were polished using diamond paste down to 1 μm. Keller's solution was used for the etching of the Al side while the Cu was etched using 100 mL of distilled water, 4 mL of saturated sodium chloric, 2 g of potassium dichromate, and 5 mL sulfuric acid. Optical micrographs were made with a Nikon Epiphot 200 microscope. SEM was made using a Zeiss Ultra 55 field emission scanning electron microscope. EDS line analysis was done using the same equipment.

Hardness Microhardness measurements of a cross section of the weld were made using a CSM microcombi tester. Four hundred fifty-one indentations were made with an indentation load of 0.5 N. The measurement matrix covered a 20 mm by 5 mm area containing the different weld zones and base materials present in the weld. The Oliver and Pharr [22] measurement method was used to determine the equivalent hardness Vickers of the indentations.

Mechanical testing (tensile and bending) The tensile tests were conducted using an MTS 858 Table Top System with resulting specimens presented in Fig. 7a. A 25 mm

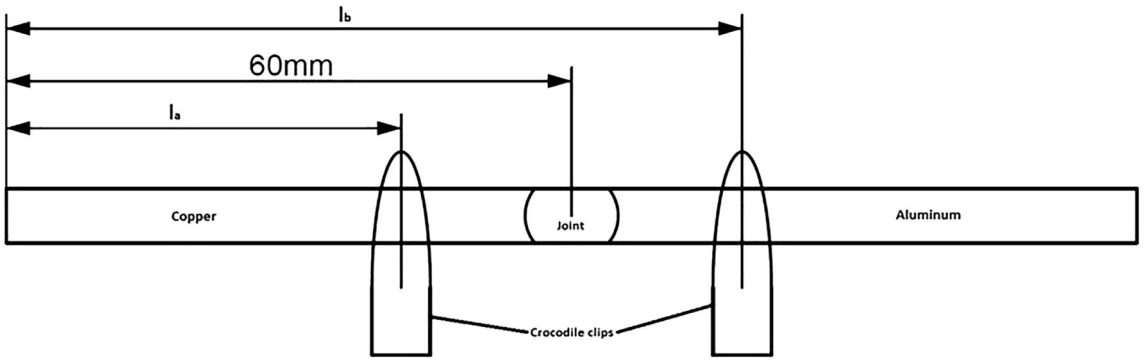

Fig. 8 Schematic representation of the electrical resistance measurement apparatus. Each of the specimens has a dimension of 5 mm (width) × 6 mm (thickness) × 60 mm (length)

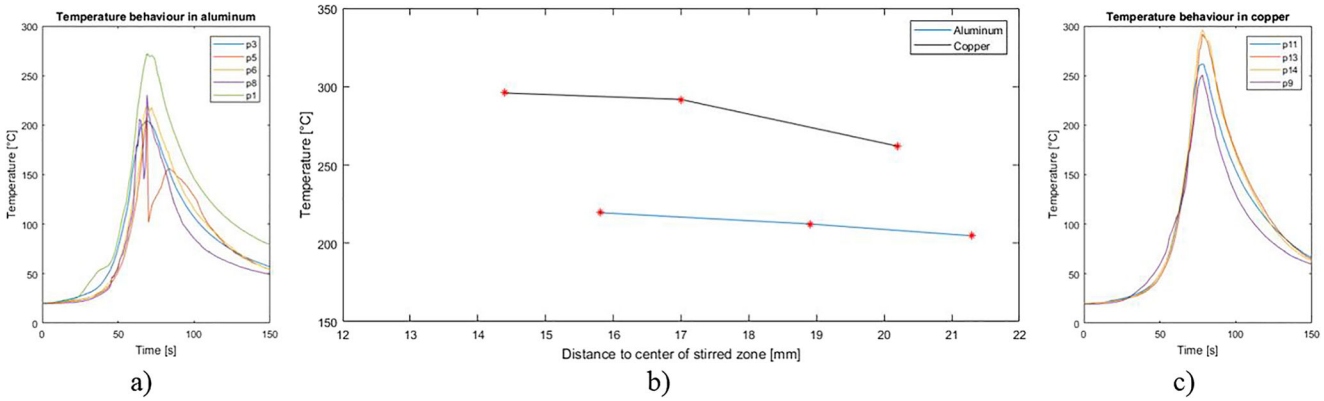

Fig. 9 Temperature monitoring results: (a), (c) temperature history at the Al side and Cu side, respectively; (b) peak/maximum temperatures at different distances from the center of the stirred zone at both the Al side and Cu side

extensometer was used for registering the strain rate. Test speed for all tests was 1 mm/min. The bending test implemented was a 3-point bend testing as represented in Fig. 7b. Tests were made for each side of the weld seam under tensile load, root, and face, using an MTS 810 Material Test System at a constant speed of 10 mm/min. The distance between the supporting rollers was 78 mm.

To assess the mechanical performance of the dissimilar Al-Cu joints, two performance parameters were used: global efficiency to tensile strength (GETS), Eq. (1); and global efficiency to bending (GEB), Eq. (2). The GETS and GEB combine the ratio of the various tensile and bending properties of the weld zone to those of the base material [23]. In this work, the mechanical properties of the weld zone are compared to those of the AA1050-H14/24. The linear combination factors presented in Eqs. (1) and (2) were selected to put emphasis on the ductility of the joints over their strength and so the performance parameters are as follows:

$$GETS_{weld} = 0.05\frac{E_{weld}}{E_{BM}} + 0.2\frac{\sigma_{y\_weld}}{\sigma_{y\_BM}} + 0.2\frac{\sigma_{UTS\_weld}}{\sigma_{UTS\_BM}} + 0.25\frac{A_{weld}}{A_{BM}} + 0.3\frac{U_{T\_weld}}{U_{T\_BM}} \quad (1)$$

$$GEB_{weld} = 0.4\frac{F_{weld}}{F_{BM}} + 0.3\frac{d_{weld}}{d_{BM}} + 0.3\frac{U_{B\_weld}}{U_{B\_BM}} \quad (2)$$

where in the GETS, the E is the Young modulus (based on Hooke Law $\sigma = k\varepsilon$); σ_y is the yield true stress (offset of 0.2%); σ_{UTS} is the ultimate true stress; A is the percent elongation at fracture in 50 mm; and U_T is the toughness ($U_T = \int_{\varepsilon_0}^{\varepsilon_f} \sigma\, d\varepsilon$, determined based on approximation of stress-strain curve with rigid-plastic Ludwik Law: $\sigma = k\varepsilon^n$). True stress (σ) and true strain (ε) values are obtained from the engineering stress, $S = \frac{F}{A_0}$, and engineering strain $d\varepsilon = dl/l \Leftrightarrow \varepsilon = \ln(e+1)$ considering $\sigma = S(e+1)$ and $\varepsilon = \ln(e+1)$. And in GEB, the F is the maximum load; d is displacement at maximum load; and U_B is the consumed energy (corresponding to the area below the F versus d graphic plot) until maximum load has been reached.

Electrical resistance testing The electrical resistance of the joint was measured and evaluated using a Cropico D07 microhmmeter. Resistance between two points on each side of the weld was measured and then the resistance contribution of the base materials subtracted to acquire the joint electrical resistance, R_{joint}, as established in Eq. (3) in according to formulation presented in [24]. See Fig. 8 for further clarification.

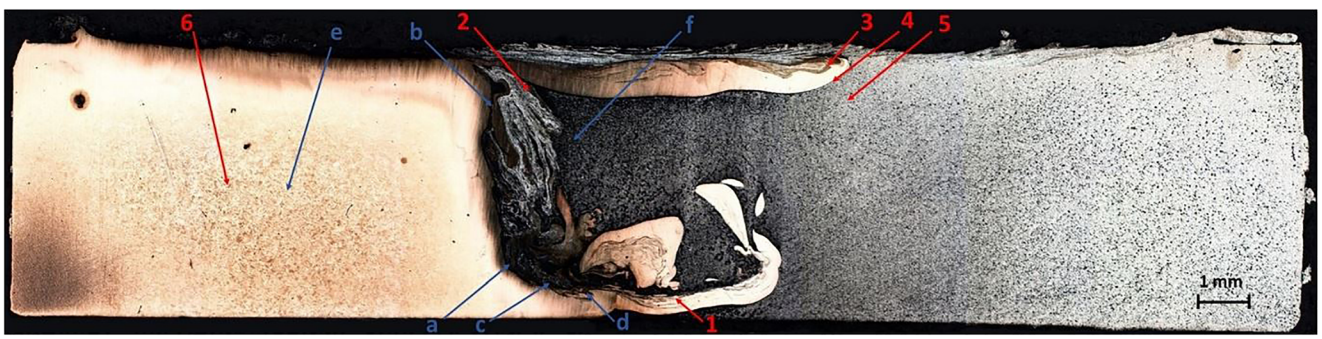

Fig. 10 Optical macrograph of the bimetallic FSW Al (right side and retreating side of the weld)–Cu (left side and advancing side of the weld) joint, with the areas marked from "1" to "6" detailed in the optical micrographs of Fig. 11 and areas marked from "a" to "f" detailed in the SEM micrographs of Fig. 12

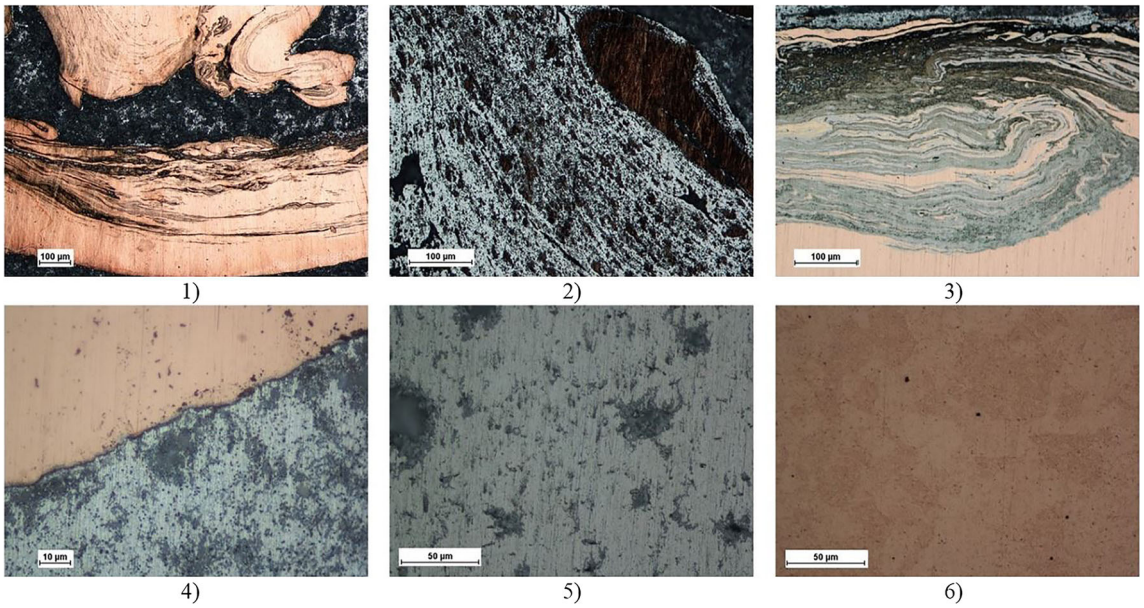

Fig. 11 Optical micrographs of the joint in Fig. 10 from positions "1" to "6": (1) Cu-rich mixed material at the Cu "tongue" near the root of the weld joint; (2) intercalated lamellae structure; (3) multilayered structure at the Cu "tongue" near the face of the weld joint; (4) intermetallic layer; (5) microstructure at the heat-affected zone of the Al; (6) microstructure at the heat-affected zone of the Cu

The length of the electrical resistance specimens was 60 mm, and their cross section was 5 mm (width, aligned with the RD) × 6 mm (thickness).

$$R_{Joint} = R_{Measured} - \frac{(60 - l_a)\rho_{Cu}}{w_{Cu}t_{Cu}} - \frac{(l_b - 60)\rho_{Al}}{w_{Al}t_{Al}} \quad (3)$$

where ρ_{Cu} and ρ_{Al} are the resistivity (μΩ mm) of Cu and Al, respectively; l is the length as depicted in Fig. 8; w is the width, and t is the thickness of the cross section of the electrical resistance specimen.

To assess the performance of the dissimilar Al-Cu FSW joints, also the electrical conductivity efficiency (σ_{eff}), as defined in the Eq. (4), based on the [24], was considered as a performance parameters.

$$\sigma_{eff} = \frac{R_{Al} + R_{Cu}}{R_{Al} + R_{Cu} + R_{Joint}} \quad (4)$$

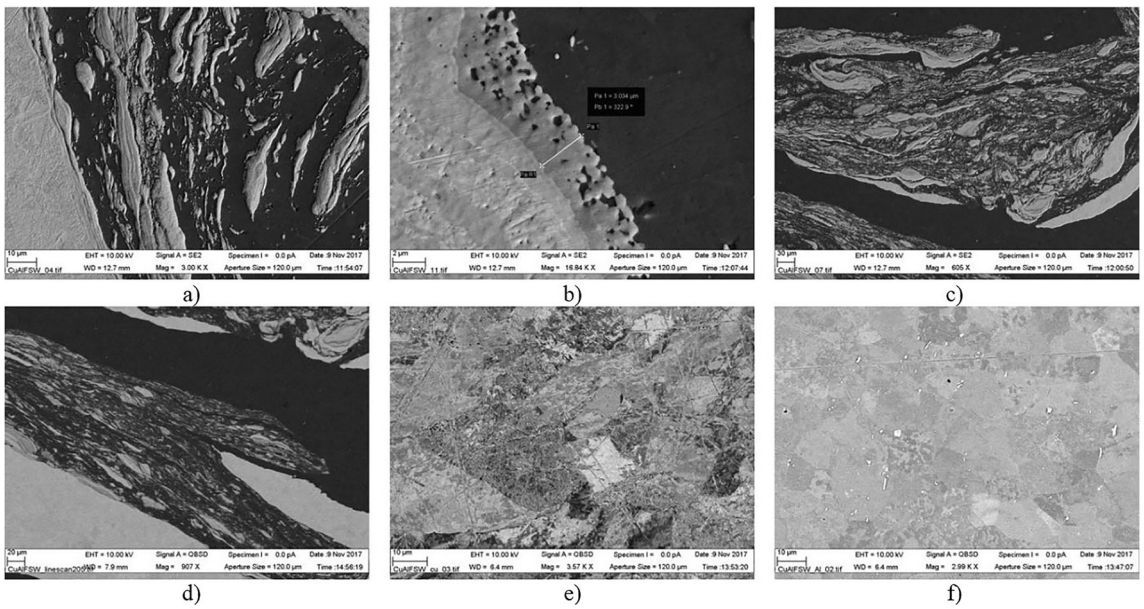

Fig. 12 SEM micrographs of the joint in Fig. 10 from positions "a" to "f": (a) Al-based composite matrix; (b) IMC layer at the Al-Cu interface; (c) intercalated lamellae structure; (d) multilayered structure at the Cu "tongue" near the root of the weld joint; (e) microstructure at the heat-affected zone of the Cu; (f) Al microstructure with Cu particles in the stirred zone

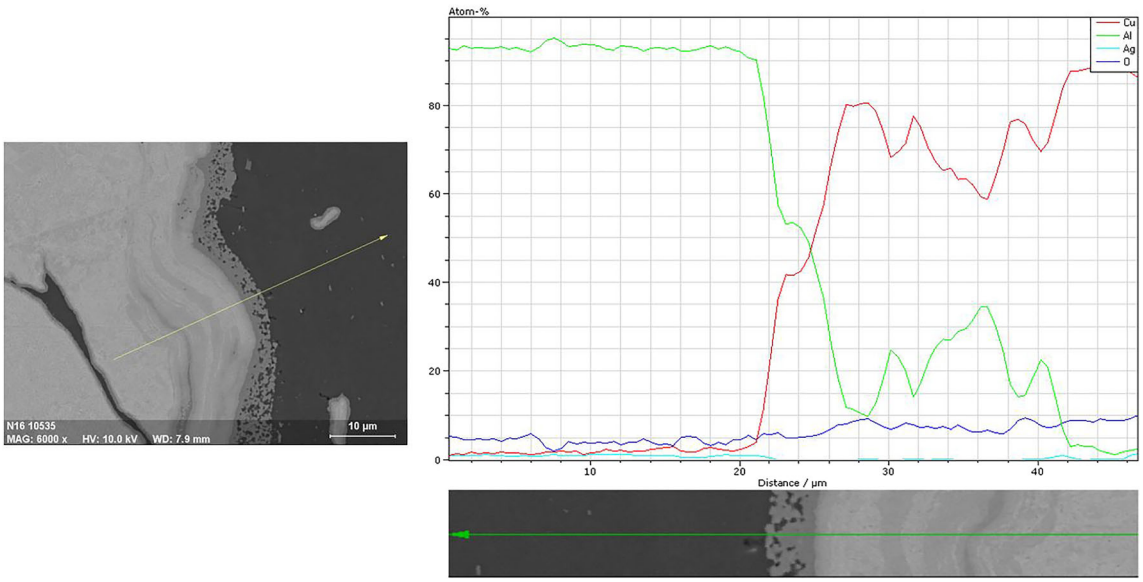

Fig. 13 EDS chemical composition analysis of the Al-Cu interface, presented in Fig. 12(b)

where R_{Al} and R_{Cu} are the electrical resistances of the Al and Cu, respectively, measured in a 12 mm long segment of each of the Al and Cu base materials, with 5 mm by 6 mm cross section.

The contact electrical resistance between the Al and Cu base materials was also measured with no weld joint, using different contact forces. This research action enables to compare it with the welded condition, and to evaluate the impact of the clamping force relaxation of bolted joints in the operation of the busbars. The Al and Cu base materials were cut into samples having the same 5 mm × 6 mm cross section as the weld specimens and their contacting ends were milled. Then they were clamped together using a vice and the electrical resistance over the contact measured for low, medium, and high forces. The lowest force was so that the samples would stay in place but could easily be moved by hand. Medium force was about 25 kN, the level of force measured at the end of the clamping force relaxation of bolted joints (Fig. 4). The high force was about 40 kN, corresponding to the considered maximum clamping force of bolted joints.

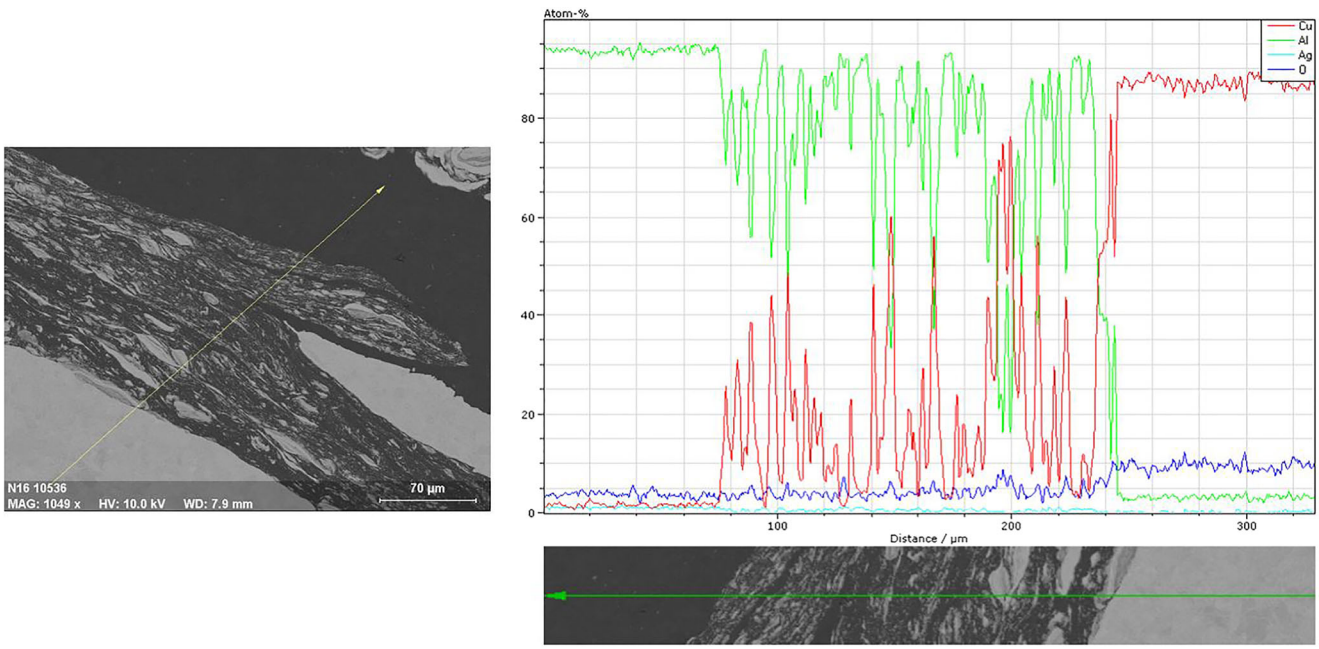

Fig. 14 EDS chemical composition analysis of the Al-Cu interface, presented in Fig. 12(d)

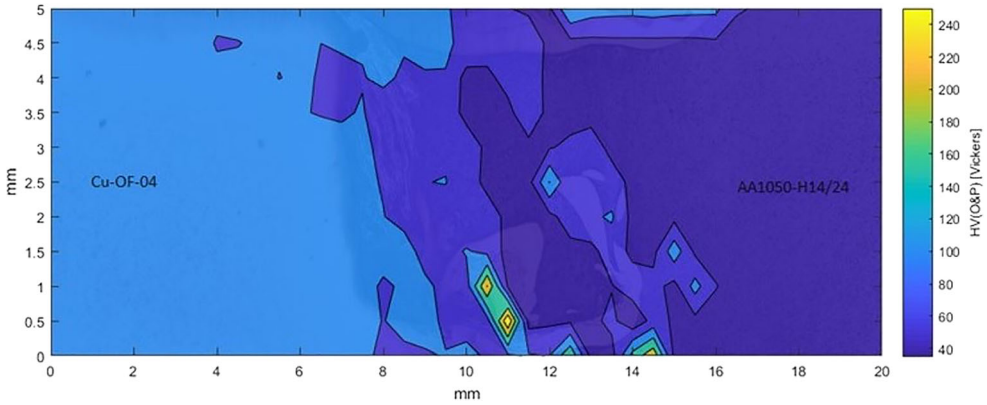

Fig. 15 Microhardness field of the FSW joint cross section, with the optical macrograph transparent in the background. The indentation load applied was 0.5 N

4 Analysis of results

4.1 Temperature monitoring

The monitoring of the temperature evolution in this bimetallic Al-Cu joint contains relevant information on the scope of the fundaments of the heat generation in FSW. The temperature history of points at the same distance from the center of the stirred zone of the base materials differ during welding. The main facts are:

1. Most of the tool is over the Al plate, due to the lateral 1.4 mm offset into the Al side;
2. The maximum temperatures reached in the Cu side are significantly higher than in Al side, especially for the thermocouples closer to the center of the stirred zone. As an example, the maximum temperature in Cu at 15.8 mm distance from the center of the stirred zone is 293.7 °C while the maximum temperature in Al at the same distance from the stirred zone is 219.5 °C.

These facts emphasize that differently from what some authors consider in their heat generation models [4, 25], the bulk of the heat is not generated due to the friction dissipation at the sliding interfaces, but in the internal energy dissipation inherent to the viscoplastic deformation of the material flow imposed by the tool geometry. As a matter of fact emphasized by the present results, the heat generated in the Cu is significantly higher than the heat generated in the Al, because for the Cu to reach the viscoplasticity, it dissipates more heat energy than the Al, because the Cu toughness is higher than the Al toughness. Moreover, the higher conductivity of the Cu reduces this temperature difference, as it homogenizes the thermal gradient faster than the aluminum. So, the monitored temperature difference is even more relevant due to the difference in thermal conductivity.

The highest temperature reached in the Al side is at p1 (Fig. 9a), which is at the start of the weld. This is due to the pre-heat generated during the plunging and dwell period. Because travel speed has not started yet, and only tool rotation exists, with no significant material flow, the heat generated is mostly generated by interfacial sliding friction and axisymmetric. Also, the close vicinity of the edge of the plates does limit the heat losses. With the tool position offset used in the process, the probe is in more contact with the Al side and heats it up more than the Cu side at the start of the weld.

4.2 Microstructure analysis: OM, SEM, and EDS

The optical macrograph of the weld, presented in Fig. 10, shows the mixture of the original Cu and Al components, resulting from the stirring effect of the FSW tool. The layer of Al transported and left behind by the travelling and rotating tool shoulder, which is noticeable at the face of the weld in Fig. 5c, is very thin and overlaps a thicker Cu layer. The Cu involves the aluminum by two "tongues" near the face and root, in a quasi "U" shape. Several regions with intercalated lamellae, diffusion, and formation of IMCs are possible to identify. The most interesting metallurgical regions, possible to identify in the optical macrograph, are selected to be depicted for analysis in optical micrographs (numbers *1* to *6* in Fig. 10) and SEM micrographs (letters *a* to *f* in Fig. 10), presented in Fig. 11 and Fig. 12, respectively.

Different Al-Cu interaction patterns can be identified such as intercalated lamellae in Fig. 11(2) and Fig. 12(c). This morphology usually consists of two or more

Table 2 Tensile properties, with standard deviation, of the FSW joint, including the performance factor global efficiency to tensile strength (GETS)

E (GPa)	σ_y (MPa)	σ_{UTS} (MPa)	A (%)	U_T (J/mm^2)	GETS
90.54 ± 2	64.09 ± 2.9	90.14 ± 4.3	26.80 ± 4.8	4.32 ± 1.6	0.85 ± 0.1

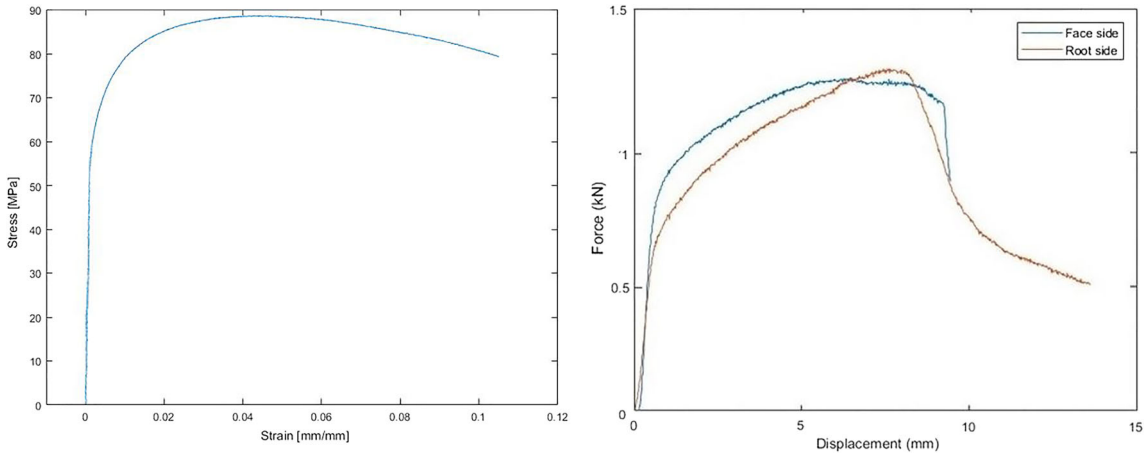

Fig. 16 Average results from the mechanical testing: (a) engineering stress-strain curves from the tensile test; (b) bending force–displacement curves from the 3-point bending tests with face and root under tensile stress condition

IMC phases and the formation is deeply influenced by process parameters such as rotational speed and lateral tool offset as reported by Galvão *et al.* [19] and Liu *et al.* [26]. Possible composite-like structures composed of Cu, Cu-rich, or IMC particles dispersed in an Al or Al-rich matrix are emphasized in Fig. 12(a). Interface layers of Al-Cu are focused in Fig. 11(4) and Fig. 12(b). The darker gray layer next to the bulk Al in Fig. 12(b) was measured, and found to have a thickness of 6 μm.

The EDS was applied to the Al-Cu sample to investigate the mixing of materials in the weld-stirred zone, with corresponding chemical composition at some representative Al-Cu interfaces. Fig. 13 and Fig. 14 present the chemical composition obtained with EDS line analysis of the Al-Cu interface focused in Fig. 12b and multilayered structure depicted in Fig. 12d, respectively. Efficient mixing and interlocking of Cu and Al is important to secure the mechanical strength of the weld. Uniform mixture of the metals improves also the heat transfer rate from the Cu plate to the channel. Possible gaps and non-mixed oxide layers reduce the resistance and electrical conductivity of the weld-stirred zone [16].

The evolution of the chemical composition obtained via EDS, at two Al-Cu interfaces with distinct patterns, is presented in Fig. 13 and 14. Based on the EDS, analysis is not possible to confirm the presence of IMC, but from the results of the chemical composition in Fig. 13, maybe Cu_3Al_2 (δ) and Al_2O_3 can be present. Also in Fig. 13, at the Cu base metal, from 28 to 42 μm, there is a solid solution of Al in Cu, similar to the one also reported by Galvão et al. [27]. The line analysis in Fig. 14 depicts a mixed structure with multiple islands of Al and Cu along a distance from 70 to 250 μm. Thus, the multilayered structure at the Cu "tongue" near the root of the weld joint zone is well interlocked. The chemical composition changes in multilayered structure from 100% Al to about 70% Cu. This indicates that the weld is potentially strong mechanically. Again, although the EDS analysis is not conclusive in the identification of IMC, considering the maximum solubility of Al in Cu of about 19.7% of at. content [28], the transition interface near the Cu-rich zone may include the α phase peritectoid intermetallic compound $AlCu_4$ (with at. Cu content of about 77%).

4.3 Hardness testing

Figure 15 shows the clear difference in the hardness of the base materials, on each side of stirred zone. The Cu presents a microhardness of about 90 HV while the Al presents microhardness around 40 HV. The stirred zone itself has a more complex distribution of hardness. Cu "tongues" near the face and the root and IMC particles, with higher hardness, enter the Al and result in the locally higher hardness fields within the softer Al. IMCs mostly localized at the bottom of the stirred zone cause the spikes in the microhardness seen there while the other mixed regions closer to the Cu have microhardness values in between that of the base materials.

Table 3 Bending properties of the FSW joint, with the root and the face of the weld joint under tensile condition, including the performance factor global efficiency to bending (GEB)

Side under tensile	F_{max} (kN)	$d_{@Fmax}$ (mm)	U_B (J/mm^3)	GEB	$GEB_{average}$
Face	1.28	6.56	6.64	0.396	0.408 ± 0.02
Root	1.31	7.55	7.26	0.419	

Table 4 Electrical resistance properties of the FSW joint *versus* a perfect electrical resistless joint

Joint resistance (μΩ)	Proportional increase (%)	σeff (%)
0.55 ± 0.1	2.9 ± 5	0.97 ± 0.05

4.4 Mechanical testing: tensile and bending loaded conditions

A summary of the results from the tensile tests is presented in Table 2. The table shows an average performance of GETS = 85% corresponding to a stress-strain exhibited in Fig. 16a. The tensile specimens presented a relatively high elongation (26.8%) with fracture at the Al side of the weld (Fig. 7a), in the heat-affected zone (HAZ).

There is small difference in the bending properties of the two sides of the joint, the root side being more efficient. The results from the bending tests show GEB as 41%. Figure 16 displays the bending stress-strain curves from the bending tests made for both directions and the bending properties of the weld can be seen in Table 3.

4.5 Electrical resistance of the joint: welded and compressed not-welded conditions

The joint resistance measured, and presented in Table 4, is very small compared to the contact resistance between Al and Cu in clamped joints, announced by other authors [15, 29]. This amount of resistance cannot be measured using normal electrical multimeters and is almost negligible as the resistance is only around 3% higher than for a perfect electrical resistless joint. The FSW joint proved to be capable of transferring electricity with minimal to negligible power losses. To evaluate with precision under the same material and geometrical conditions, the contact electrical resistance between the same 6 mm × 5 mm cross section surfaces of Cu-OF-04 and AA1050-H14/24 while subjected to various force levels was evaluated and presented in Table 5. The resistance of the FSW joint is 200 times lower than the contact resistance between the base materials while under an high clamping force, corresponding to the maximum clamping force of bolted joints (about 40 kN), considered in the evaluation of the clamping force relaxation presented in "Evaluation of the clamping force relaxation." Together, Table 1, Table 4, and Table 5 emphasizes the significant operational benefit of Al busbar with FSWelded Cu ends. This is a fact because the contact resistance increases significantly with the drop of the clamping force (e.g., about three times from 40 to 25 kN of clamping force drop), and the Al ends present a significantly higher rate of relaxation of the clamping force compared with the Cu ends (e.g., two times faster for ΔF/cycle@100–200 first thermal cycles).

Table 5 Contact electrical resistance (without weld joint) between 6 mm × 5 mm cross section surfaces of Cu-OF-04 and AA1050-H14/24 while subjected to various compressive contact force levels

Contact force (levels)	Contact resistance (μΩ)
~ 5 N (low)	8000 ± 2000
~ 25 kN (medium)	340 ± 30
~ 40 kN (high)	110 ± 30

5 Conclusions

The investigation of the bimetallic FSW joint between the plates with thickness of 6 mm, made of AA1050-H14/24 and Cu-OF-04 FSW, with the manufacturing of Al busbar with welded Cu ends in mind, delivered the following main results:

- The monitoring of the temperature disclosed that even though most of the tool is over the Al plate, due to the lateral 1.4 mm offset into the Al side, the maximum temperatures reached in the Cu side are significantly higher than in Al side. For example, at 15.8 mm distance from the center of the stirred zone, maximum temperature in Cu is 293.7 °C, while the maximum temperature in Al is 219.5 °C. These facts emphasize that the bulk of the heat is not generated due to the friction dissipation at the sliding interfaces, but in the internal energy dissipation inherent to the viscoplastic deformation of the material flow imposed by the tool geometry;
- Metallurgical investigation of the joints shows an intense mixture of materials with large amounts of multilayered structures, both Al-matrix composite and intercalated lamellae. The Cu involves the aluminum by two "tongues" near the face and root, in a quasi "U" shape. Most of these microstructural features are possible to identify in the pattern of the hardness field;
- In terms of mechanical properties compared to the Al component, the efficiency to tensile strength was 85%, and efficiency to bending was 41%;
- FSW joints produced show a negligible electrical resistance compared to the resistance between clamped base materials. The electrical resistance of the FSW joint is 200 times lower than the contact resistance between the base materials while under the highest tested clamping force, of about 40 kN;
- A significant operational benefit of Al busbar with FSWelded Cu ends was proved. The electrical contact resistance increases significantly with the drop of the clamping force and the Al ends present a significantly higher rate of relaxation of the clamping force compared with the Cu ends, e.g., two times faster for ΔF/cycle@100–200 first thermal cycles.

Acknowledgements Open access funding provided by Aalto University.

References

1. Thomas W (1991) ""Friction stir butt welding,"" International Patent Application no.PCT/GB92/0220.
2. Lohwasser D, Chen Z (2009) Friction stir welding: from basics to applications. Elsevier, Amsterdam
3. Mishra RS, De PS, Kumar N (2014) Friction stir welding and processing: science and engineering. Springer, Amsterdam
4. Schmidt HB, Hattel JH (2008) Thermal modelling of friction stir welding. Scr Mater 58(5):332–337
5. Murugan B, Thirunavukarasu G, Kundu S, Kailas SV, Chatterjee S (2018) Interfacial microstructure and mechanical properties of friction stir welded joints of commercially pure aluminum and 304 stainless steel. J Mater Eng Perform 27(6):2921–2931
6. Shen Z, Chen Y, Haghshenas M, Gerlich A (2015) Role of welding parameters on interfacial bonding in dissimilar steel/aluminum friction stir welds. Engineering Science and Technology, an International Journal 18(2):270–277
7. Sorger G, Wang H, Vilaça P, Santos TG (2017) FSW of aluminum AA5754 to steel DX54 with innovative overlap joint. Weld. World 61(2):257–268
8. Mehta KP, Badheka VJ (2016) A review on dissimilar friction stir welding of copper to aluminum: process, properties, and variants. Mater Manuf Process 31(3):233–254
9. Vilaça P, Mendes J, Nascimento F, Quintino L (2016) Application of FSW to join aluminium foil winding coils for electrical transformers. Int J Mech Syst Eng 2(1):115–111
10. Pruitt BL, Park W, Kenny TW (2004) Measurement system for low force and small displacement contacts. J Microelectromech Syst 13(2):220–229
11. Sullivan CR (2008) Aluminum windings and other strategies for high-frequency magnetics design in an era of high copper and energy costs. IEEE Trans Power Electron 23(4):2044–2051
12. W. S. Loewenthal and D. L. Ellis, ""Fabrication of GRCop-84 rocket thrust chambers,"" 2005.
13. Davis JR, Davis JR (1993) Aluminum and aluminum alloys. ASM international, Cleveland
14. Nix F, MacNair D (1941) The thermal expansion of pure metals: copper, gold, aluminum, nickel, and iron. Phys Rev 60(8):597
15. Jackson R (1982) Electrical performance of aluminium/copper bolted joints. In: IEE Proceedings C (Generation, Transmission and Distribution), pp 177–184
16. Napieralska-Juszczak E, Komeza K, Morganti F, Sykulski JK, Vega G, Zeroukhi Y (2017) Measurement of contact resistance for copper and aluminium conductors. Int J Appl Electromagn Mech 53(4):617–629
17. DebRoy T, Bhadeshia H (2010) Friction stir welding of dissimilar alloys–a perspective. Science and Technology of Welding and Joining 15(4):266–270
18. Schulze GE (2013) Metallphysik: Ein Lehrbuch. Springer-Verlag, Berlin
19. Galvao I, Oliveira J, Loureiro A, Rodrigues D (2011) Formation and distribution of brittle structures in friction stir welding of aluminium and copper: influence of process parameters. Science and Technology of Welding and Joining 16(8):681–689
20. Khodir S, Ahmed M, Ahmed E, Mohamed SM, Abdel-Aleem H (2016) Effect of intermetallic compound phases on the mechanical properties of the dissimilar Al/Cu friction stir welded joints. Journal of Materials Engineering and Performance 25(11):4637–4648
21. Ólafsson D (2017) ""Friction stir welding of aluminum - copper"". Aalto Master thesis.
22. Oliver WC, Pharr GM (1992) An improved technique for determining hardness and elastic modulus using load and displacement sensing indentation experiments. J Mater Res 7(6):1564–1583
23. Vilaça P, Thomas W (2011) Friction stir welding technology. In: Structural Connections for Lightweight Metallic Structures. Springer, Berlin, pp 85–124
24. Farrell T (2012) Chapter 2 - Measurement techniques. In: The Handbook of electrical resistivity: new materials and pressure effects by G. Dyos, The institution of Engineering and Technology, pp 11–24
25. Neto DM, Neto P (2013) Numerical modeling of friction stir welding process: a literature review. The International Journal of Advanced Manufacturing Technology 65(1-4):115–126
26. Liu HJ, Shen JJ, Xie S, Huang YX, Cui F, Liu C, Kuang LY (2012) Weld appearance and microstructural characteristics of friction stir butt barrier welded joints of aluminium alloy to copper. Science and Technology of Welding and Joining 17(2):104–110, February 01
27. Galvão I, Loureiro A, Rodrigues DM (2016) Critical review on friction stir welding of aluminium to copper. Science and Technology of Welding and Joining 21(7):523–546, October 02
28. Murray JL (1985) The aluminium-copper system. International Metals Reviews. 30(1):211–233
29. Bonwitt W (1948) An experimental investigation of the electrical performance of bolted aluminum-to-copper connections. Transactions of the American Institute of Electrical Engineers 67(2):1208–1219